

An Integrated Statistical Investigation of Internal Carotid Arteries of Patients Affected by Cerebral Aneurysms

TIZIANO PASSERINI,¹ LAURA M. SANGALLI,² SIMONE VANTINI,² MARINA PICCINELLI,¹
SUSANNA BACIGALUPPI,^{3,4} LUCA ANTIGA,⁵ EDOARDO BOCCARDI,⁶ PIERCESARE SECCHI,²
and ALESSANDRO VENEZIANI¹

¹Department of Mathematics and Computer Science, Emory University, Atlanta, GA, USA; ²MOX, Modeling and Scientific Computing, Department of Mathematics, Politecnico di Milano, Milan, Italy; ³Department of Neurosurgery, Niguarda Ca'Granda Hospital, Milan, Italy; ⁴Department of Neurosciences and Biomedical Technologies, University of Milano-Bicocca, Monza, Italy; ⁵Orobix, Bergamo, Italy; and ⁶Department of Neuroradiology, Niguarda Ca'Granda Hospital, Milan, Italy

(Received 30 April 2011; accepted 14 December 2011; published online 28 December 2011)

Abstract—Cerebral aneurysm formation is the result of a complex interplay of systemic and local factors. Among the latter, the role of the geometry of the vessel hosting an aneurysm, of the upstream vasculature and the induced hemodynamics still need to be carefully investigated. In this paper we combine computational fluid dynamics analysis and morphological characterization and carry out the statistical investigation of the features of the internal carotid artery (ICA) of 52 patients affected by a cerebral aneurysm. The functional principal component analysis performed on the geometric and fluid dynamics features of the patients reveals correlations with the location of the aneurysm in the cerebral circulation and its rupture status. This allows a clustering of the patients that is anticipated to contribute to the design of an index for the rupture risk. In particular, ICA featuring a pronounced WSS peak are statistically inclined to hosting ruptured aneurysms. Moreover, our statistical results suggest that patients with a double-bend siphons (*S*-class) are less prone to the development of cerebral aneurysms.

Keywords—Cerebral aneurysms, Image processing, Computational fluid dynamics, Functional principal component analysis.

INTRODUCTION

Cerebral aneurysms formation is considered the result of the complex interplay among systemic effects, the biomechanical properties of the vessel wall and the

continuous effect of forces exerted by blood flow on the vessels.^{8,19,37,39}

While systemic factors influencing the development of the pathology such as genetic conditions, smoking, hypertension and familial predisposition affect the whole arterial vasculature, cerebral aneurysms tend to occur in regions with particular features such as bends and bifurcation apexes. This clinical evidence supports the hypothesis of a major involvement of hemodynamics in the aneurysms pathophysiology. However the underlying mechanisms triggering the onset of the disease still need to be identified and explained, as well as the specific factors causing some lesions to rupture. This is a particularly challenging task, given the inter-individual variability of the cerebro-vascular districts, the simultaneous presence of different relevant factors and the difficulty of collecting crucial information, in particular follow up observational studies that could provide insights into the history of unruptured aneurysms. On the other hand the accomplishment of this task would result in the definition of reliable rupture risk indexes, that would potentially provide a mean to stratify aneurysms according to their probability of bleeding and support clinicians in the critical management of unruptured lesions.³⁸

In the last decades the focus of computational fluid dynamics (CFD) studies has mainly concentrated on the intra-aneurysmal flow features and wall shear stress (WSS) distributions on the sac dome^{7,9,14,37} and on the extraction of morphological indexes of aneurysm sac shape and size.^{10,28,42} Recently some authors have underlined the importance of the modeling and characterization of aneurysm parent vasculature. Castro *et al.*⁶ studied the influence on intra-aneurysmal flow of the portion of the upstream parent vessels included in the computational domain; Imai *et al.*¹³

Address correspondence to Alessandro Veneziani, Department of Mathematics and Computer Science, Emory University, Atlanta, GA, USA. Electronic mail: tiziano@mathcs.emory.edu, laura.sangalli@polimi.it, simone.vantini@polimi.it, marina@mathcs.emory.edu, susannabacigaluppi@yahoo.it, luca.antiga@gmail.com, Edoardo.Boccardi@OspedaleNiguarda.it, piercesare.secchi@polimi.it, ale@mathcs.emory.edu

and Sato *et al.*³⁵ demonstrated by means of parametric studies on idealized models that different degrees of torsion of the feeding artery remarkably affect inflow patterns and flux; Hoi *et al.*¹² parametrically studied the effect of the parent artery curvature and found that flow impingement area linearly grows with the parent artery curvature. An image-based detailed analysis of the geometric features related to the location and rupture of lateral aneurysms developing along the internal carotid artery (ICA) has been carried out by Piccinelli *et al.*,²⁴ which is the observational study that has created the ground for this work.

Nevertheless, investigations on the relationship between three dimensional (3D) morphology of patient-specific vasculature and hemodynamics still have to face many challenges: primarily, real anatomies display very large variability, especially in the intracranial vasculature, and the retrieval of 3D geometric features in a robust and operator-independent way is a developing but not yet established field; secondly, a quantitative analysis of integrated datasets including geometric information and hemodynamics results is to the authors' knowledge a rather new field that requires the application and development of *ad hoc* tools.

This paper aims at giving a contribution in this direction with two distinctive features, one refers to the specific subject of our investigation, the other one to the methods adopted for the data analysis.

1. The focus of our study is the quantitative and computational characterization of the geometry and hemodynamics of the ICA comparing features of ICAs harboring aneurysms with features of ICAs of subjects with aneurysms in a downstream location or no aneurysms at all. Vessel geometry has been recognized as a relevant factor in vascular pathologies since a long time, but a precise and quantitative analysis of the geometry of intracranial arteries as preferred sites of development of aneurysms is still insufficient.²⁴ On the other hand, CFD studies usually focus on aneurysmal flow rather than on a characterization of the feeding arteries. The vessel geometry is here characterized by means of radius and curvature, while wall shear stress (WSS), its axial gradient and blood energy drop along the ICA path are considered as surrogate measures of hemodynamics features.
2. Heterogeneity and variability of the data at hand demand for sophisticated statistical methods. Our dataset comprises both geometry and fluid dynamics: these quantities are regarded as stochastic functions of an axial coordinate defined along the vessel. To extract patterns from such a complex aggregate of

information we resorted to advanced statistical techniques, namely the *functional principal component analysis* (FPCA). These methods allow to identify the part of the data set relevant for our purposes, i.e. the detection of recurrent patterns in geometry and/or fluid dynamics that may relate to the presence of the pathology and a lesion rupture event.

The ground of this work is the integration of different types of information—from the radiological acquisition, to the 3D reconstruction of patient-specific anatomies and their geometric characterization, the CFD modeling and the statistical analysis of the comprehensive dataset—with the ultimate goal of devising rupture risk indexes with diagnostic and possibly prognostic purposes, as explained in Piccinelli *et al.*^{24,25} and Sangalli *et al.*^{31,32}

The results presented here show that geometrical features such as the radius of the ICA, its curvature and the axial derivative of the WSS have a significant correlation with the rupture status of the aneurysms in our data set. As a matter of fact, the FPCA extracts from those quantities the part (or more precisely the *principal component*) actually related to the rupture. In particular, patients with unruptured aneurysm in the ICA or without aneurysms (up to the neuroradiological evidence) feature a double-bend siphon as opposed to patients with ruptured or distal aneurysms, presenting preferentially a single-bend siphon. Moreover, pronounced peaks of WSS are statistically related to ruptured aneurysms in the ICA. These findings provide a further justification for the pre-existing clustering of patients into two classes, Ω and S groups depending on the shape of the siphon. In particular, we found that patients in the group S are more protected from the development of the pathology.

We argue with statistical evidence that the different behavior in the two cases is related to the different level of energy loss in the ICA, induced by the bends.

The paper is organized as follows. In “[Materials and Methods](#)” section we describe the components of our methodological workflow: the reconstruction of 3D models and their geometric characterization, the CFD modeling and the statistical tools employed. “[Results](#)” section illustrates the results obtained after the statistical analysis. A phenomenological discussion is carried out in “[Discussion](#)” section.

MATERIALS AND METHODS

The Data Set

The data set of the present study consists of 52 patients who underwent 3D-RA for cerebral aneurysm

assessment following clinical routine at the Neuroradiology Division of the Niguarda Ca'Granda Hospital in Milan, Italy. At admission, patients signed a consent form for the use of their personal data according to the current Italian law. The study did not imply any change in the management of the patient, nor was any additional procedure undertaken; no further IRB procedure is currently requested for using anonymized retrospective data in Italian Hospitals.

Acquisitions were performed with an Integris Allura Unit (Philips, Best, the Netherlands) with the following parameters: C-arm rotation speed, 55 per second; matrix size 512×512 ; frame rate, 25 frames per second; 18 mL nonionic hydrosoluble contrast agent was injected prior to the acquisition at 4 mL/s. The rupture status of the patient was registered by one of the authors (EB), senior radiologist of the Hospital.

The patients were subdivided into groups according to the location and the rupture status of the lesions. Moving from the results presented in Sangalli,³¹ where patients with an aneurysm located at the terminal bifurcation of the ICA or distally (group U) and patients with proximal aneurysms (w.r.t. the ICA terminal bifurcation—group L) have been demonstrated to have statistically different features (U-subjects have wider, more tapered and less curved ICAs than L patients), we added to this classification the discriminant of the rupture. More precisely we considered five classes,

UR (Upper Ruptured) subjects with a *ruptured* aneurysm *at or after* the final bifurcation of the ICA;

UN (Upper Non-ruptured) subjects with a *non-ruptured* aneurysm *at or after* the final bifurcation of the ICA;

LR (Lower Ruptured) subjects with a *ruptured* aneurysm along the ICA, *before its terminal bifurcation*;

LN (Lower Non-ruptured) subjects with a *non-ruptured* aneurysm along the ICA, *before its terminal bifurcation*;

No (No Aneurysm).

Table 1 reports the cardinality of each group as well as details on the precise localization of the lesions within each subclass. The ICA aneurysms listed under the U group are terminal aneurysms located exactly at the bifurcation.

Geometric Characterization

The reconstruction of patient-specific anatomies and part of the geometric characterization of the parent vasculature were achieved by means of the Vascular Modeling Toolkit (VMTK).⁴¹ The following operations were performed for each patient.

TABLE 1. Summary of the Aneurisk data set considered in the present study.

Group	Cardinality	Position		
		ICA	MCA	ACA
U				
UN	11	1	5	5
UR	16	1	2	13
L				
LN	13	13	–	–
LR	9	9	–	–
No	3	–	–	–
Total	52	24	7	18

1. The 3D surface model of the aneurysm and its parent vessels was reconstructed by means of a gradient-driven level-set approach²; in particular all the acquired portion of parent vasculature was included in the model.
2. The centerlines of the reconstructed vascular network were extracted³ as well as a centerline traveling through the aneurysm sac²⁴; a point-wise estimate of the vessels radius was readily available from the centerline computation techniques.²⁵
3. The vascular network bifurcations were automatically identified; the centerlines for each vascular branch tagged accordingly; the same subdivision was successively applied to the 3D surface model.²⁵
4. A curvilinear abscissa was defined traveling along the vessel: selecting the ICA bifurcation²⁵ as a landmark on all the models, this abscissa parameterized the ICA length in the upstream direction; by definition the abscissa was set to zero at the bifurcation point and assumed negative values moving upstream.

Figure 1 illustrates the geometric characterization performed on one of the patients of the data set, the 3D modeling, the split centerlines network and the corresponding subdivided surface.

Numerical Simulations

The region investigated in the present paper is the siphon of the ICA and its main bifurcation: in the 3D model, the ICA was kept entirely while the downstream circulation was properly trimmed. Cylindrical prolongations (*flow extensions*) were added at each extremal section of the surface, in such a way that the geometrical model featured circular inlet and outlet sections, corresponding to the proximal and the distal boundaries respectively. The length of these cylindrical extensions was adaptively selected as 10 times the clipped section radius.

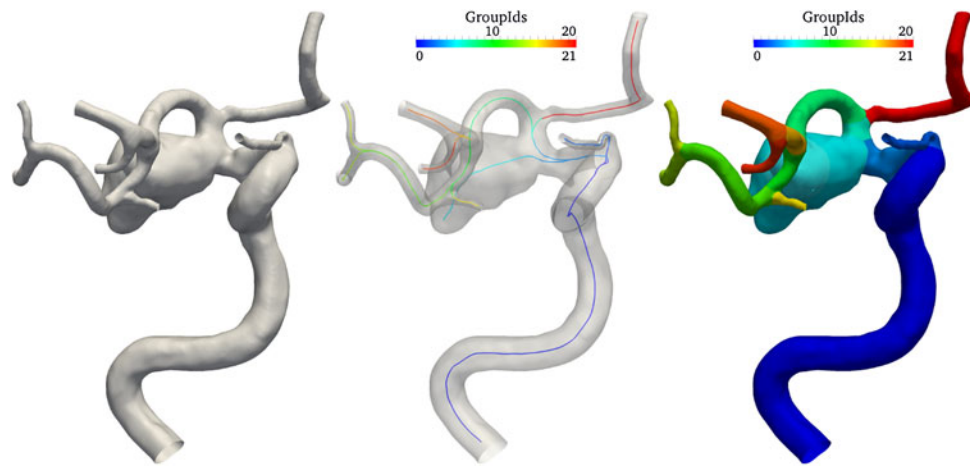


FIG. 1. Left: 3D surface model of ICA hosting an aneurysm; middle: split centerlines for the whole vascular network; right: split 3D surface model. Each vascular branch is associated to a different numeric label (GroupId)..

For each geometrical model we obtained a tetrahedral grid with an average element size of 0.6 mm using the Netgen Mesh Generator.³⁶ The size of the mesh was selected as a trade-off between the accuracy and the computational time requirements. This was clearly a delicate issue, since the present research comprised the extensive CFD analysis of a large data set of patients. We verified on a smaller sample of patients that computations over finer meshes, while significantly more intensive in terms of simulation time, did not bring major improvements to the statistical results. The considered mesh size was actually capable of capturing the patterns of the WSS relevant to the FPCA.

The computational domain was assumed to be fixed, corresponding to the common hypothesis of rigid vascular walls. We further assumed that blood can be modeled as a continuous incompressible Newtonian fluid, so that the flow problem can be described by the incompressible Navier–Stokes equations.¹¹ For each vascular geometry, three cardiac cycles were simulated, in order to reduce the effects of the initial conditions and obtain the periodic solution in the last simulated heart beat. The spatial discretization was based on the Galerkin finite element method, and was carried out with a piecewise linear approximation for both the pressure and the velocity. The numerical scheme adopted is based on an edge stabilization technique⁵ that allows equal order interpolation. The adopted time advancing scheme is a semi-implicit Euler method, with a time step of 10^{-3} s.

To estimate the WSS over the computational domain it is necessary to retrieve a suitable approximation of the velocity gradient. We used an L^2 projection method,^{4,43} which is proven to provide a superconvergent approximation of the gradient on linear elements.

An important issue is the prescription of the boundary conditions. Ideally, patient-specific boundary conditions should have been prescribed. Unfortunately,

the current clinical protocol does not include the measurement of velocity/pressure data to be used to this aim. On the other hand, the focus of the present work is on the role of the geometry of ICA as a determinant of the flow features, so we prescribed comparable realistic hemodynamics conditions to all the geometries of the data set. More precisely, we considered the Reynolds number evaluated at the inflow section as the parameter for the description of the flow regime. A time average Reynolds number of $Re = 350$ is supposed to describe realistically the flow regime in the ICA.²² Accordingly, a flat axial velocity profile was prescribed at the inflow sections, the flow rate being adjusted to yield this target Reynolds number. The selection of the arbitrary velocity profile is legitimated by using cylindrical boundary extension on the inlet section. It is indeed proven that the geometrical features of the vessel have a stronger influence on the solution than the presence of secondary motion in the inlet velocity profile.¹⁸ Moreover, the effects of inlet secondary flows, even in case they are present, break down within a few diameters of the inlet,¹⁷ featuring an exponential decay from the inlet section.⁴⁰ Pulsatility of the flow was forced by the classical waveform representative of the carotid arterial flow advocated in Osenberg,²⁰ Prosi *et al.*,²⁶ and Rappitsch and Perktold.³⁰

At the outlets usual stress-free outflow conditions were prescribed. It is worth mentioning explicitly the treatment of small collateral branches. The small branches of the ICA were included in the geometrical model whenever the image resolution allowed for their reconstruction. In some cases however they were neglected, because the image quality was not sufficient to reliably determine their geometry. The effect of the presence or absence of small ICA branches on the results presented later on is however negligible. We have verified this statement in a case in which it was possible to reconstruct the ICA geometry including a small branch. The

WSS profiles computed on the complete geometry and after artificially removing the collateral branch did not show significant discrepancies in view of the FPCA.

Post-processing

To integrate the analysis of the geometric and hemodynamics features, WSS field was properly post-processed and homogenized with the morphological data. The ICA was divided into a sequence of sections located at the curvilinear abscissas s_k such that $s_{k+1} - s_k = 2$ mm (see Fig. 2). Each section was taken orthogonal to the centerline and was corresponded by a slice \mathcal{S}_k of the surface of the vessel (represented on the left with different colors as a function of s_k). The slices were assumed to be non overlapping, and their boundaries were defined by edges of the computational grid.

For each patient we computed the local average WSS over the slice \mathcal{S}_k as a function of the curvilinear abscissa s_k and time,

$$\overline{\text{WSS}}(s_k, t) = \left\| \left\| \frac{1}{|\mathcal{S}_k|} \int_{\mathcal{S}_k} \text{WSS}(x, y, z, t) d\mathcal{S} \right\| \right\|.$$

In particular we recorded the systolic peak value $\overline{\text{WSS}}(s_k, t_{\text{sys}})$. By means of spline interpolation this quantity and its axial derivative $\frac{d\overline{\text{WSS}}}{ds}(s_k, t_{\text{sys}})$ were reformulated as a function of the curvilinear abscissa, as done for the radius and curvature of the vessel centerline.

The choice of the slice width of 2 mm was a trade-off between accuracy and computational effort. Computation of the average WSS on slices of 1 mm did not yield differences that affect significantly (from the statistical point of view) the results.

We also quantified the energy loss experienced by the blood stream when flowing through the ICA.

Energy loss in the sac has been recently proposed as a possible index for the rupture risk quantification of cerebral aneurysms.³⁸ In the present work it was estimated by computing the difference of the total mechanical energy of the fluid on two cross-sections of the vessel, located upstream (*Section U*) and downstream (*Section D*) the siphon (see Fig. 2). The downstream section was located at the terminal bifurcation of the ICA. The upstream section was located at the most proximal location available in all the considered geometries, after a proper alignment of the vessels centerlines to filter out systemic artifacts, as explained in the following paragraph.

Since the variation of gravitational potential energy is negligible, the total mechanical energy is defined as the sum of the kinetic and fluid energies, so that the energy loss reads

$$\mathcal{L}(t) = \int_{\text{Section D}} \left(\rho \frac{\mathbf{u} \cdot \mathbf{u}}{2}(t) + p(t) \right) ds - \int_{\text{Section U}} \left(\rho \frac{\mathbf{u} \cdot \mathbf{u}}{2}(t) + p(t) \right) ds$$

where ρ is the fluid density. In the sequel, we actually refer to the time averaged energy loss $\overline{\mathcal{L}}$ over a heart beat.

Numerical simulations have been carried out with in-house software based on *LifeV*,¹⁶ an open source C++ finite element library for the solution of partial differential equations in 3D on unstructured meshes, on serial and parallel architectures. Visualization of the results has been obtained with the *Paraview* free software.²¹

Statistical Analysis

The analysis of the data reconstructed from the geometry requires three main steps. In the first one we

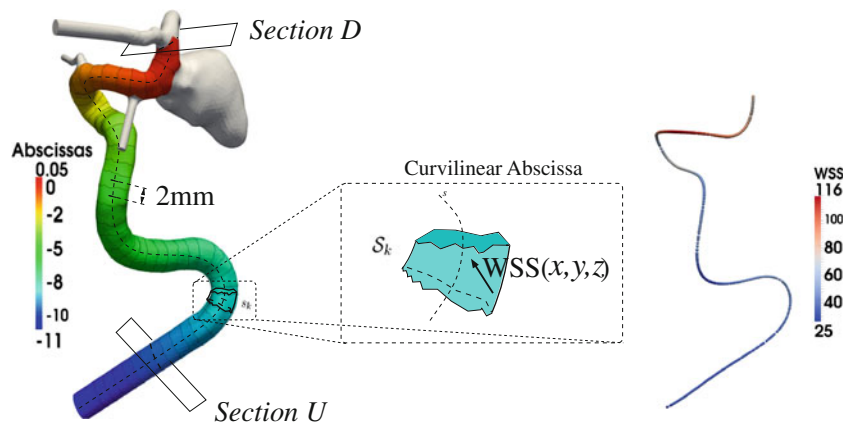


FIG. 2. Computation of the average shear stress $\overline{\text{WSS}}$ as a function of the curvilinear abscissa s . Left: the vascular surface is subdivided in slices \mathcal{S}_k , corresponding to a set of equispaced values of the curvilinear abscissas (the width of the step is 2 mm). Right: the averaged shear stress is associated to centerline points.

approximated the centerlines of each ICA reconstructed by VMTK with a smooth function. Since we were interested in the curvature of the centerline, requiring the differentiation of its parametric representation, we resorted to a functional representation based on *free-knots splines* of order 4.³²

The top left panel of Fig. 3 shows the derivatives of the three space coordinates of the estimated ICA centerlines, $\{x'(s), y'(s), z'(s)\}$, for each subject along the curvilinear abscissa. These quantities well represent the variability of our data set. The figure pinpoints a remarkable misalignment of the data. In particular we noticed a strong phase variability largely due to the different size of the body and thus of the arteries of the different patients. To filter this effect out we decoupled the *phase variability* among the subjects, strongly dependent on ICAs dimensions, from an *amplitude variability*. The latter reflects the variability in the morphological shapes of ICAs, in which we were mostly interested.³¹ The decoupling led to the alignment displayed in the right panel of Fig. 3, that could thus be profitably used for comparisons across subjects. The mean curve (template) resulting from the alignment of the different subjects is reported in the pictures as a black bold line. The template of the centerline first derivatives displayed in Fig. 3 still showed a large amplitude variability, especially at values of the abscissa between -5 and -2 cm, that required further investigation. Following the procedure illustrated in Sangalli *et al.*³⁴ we came up with two clusters (with two corresponding templates) as an accurate representation of the data set. The mean curves of the two clusters are reported in Fig. 4, right.

The two mean centerlines identified in this way are represented in 3D in Fig. 5. A similarity analysis pinpointed that two clusters are enough for capturing the variability across the data set, a 3-groups clustering being not significantly better (Fig. 4, left).

The two estimated templates identify two prototype morphological shapes of ICA that have since long time been described in medical literature.¹⁵ Namely, the dark (green) template centerline is a prototype of a so-called Ω -shaped ICA, whose siphon has just one main bend in its distal part; the light (orange) one is instead a prototype of a so-called *S*-shaped ICA, whose siphon has two main bends in the distal part.

All the data associated with the centerlines (radius, curvature, local average WSS, etc.) have been registered according to the same procedure performed for the centerlines themselves. Each variable of interest was represented therefore by a function of the registered curvilinear abscissa s along the centerline. These functions were regarded as the realization of a random process, whose features could be significantly correlated to the belonging of the subject to a specific group. The identification of such features was however made difficult by the huge complexity and variability of the data represented by these functions. FPCA pursues the goal of a reduction of the complexity of the data. Similarly to a modal or a proper orthogonal decomposition, FPCA aims at identifying a finite dimensional subspace onto which to project the functional data providing a good compromise between information loss and statistical power gain (Karhunen-Loève decomposition of the sample autocovariance operator). The identification of the most convenient basis (the set

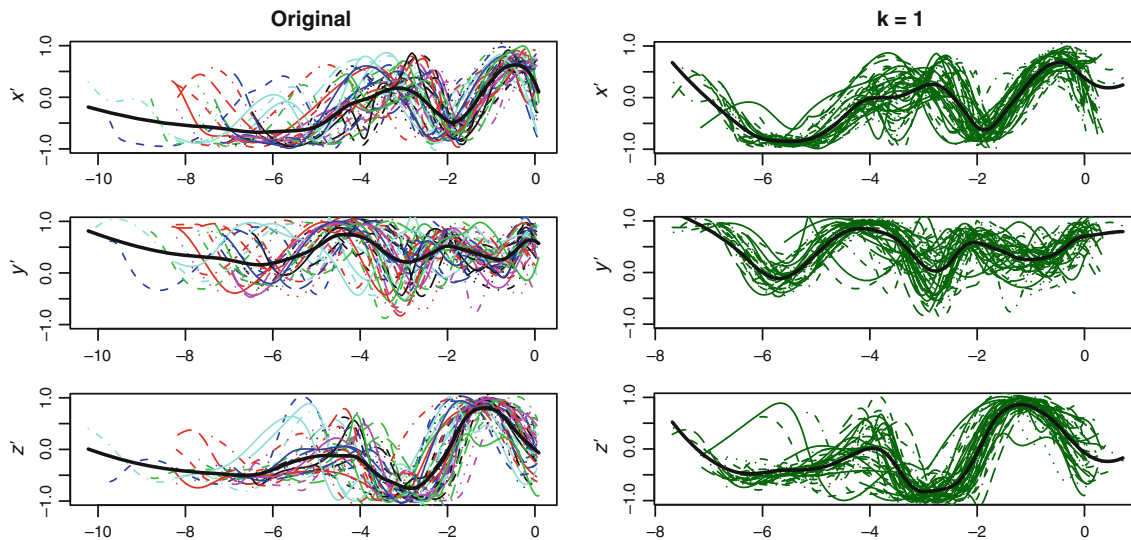


FIG. 3. Left: first derivatives with respect to the curvilinear abscissa of the centerlines coordinates ($x' = dx/ds$, $y' = dy/ds$, $z' = dz/ds$) of the estimated ICA, reconstructed from images after the free knot estimation. The black thick curve represents the template reconstructed by the data without alignment. Right: first derivatives of centerlines after the alignment. We identified here just one cluster of data ($k = 1$). The template of this cluster is represented again by the black thick line.

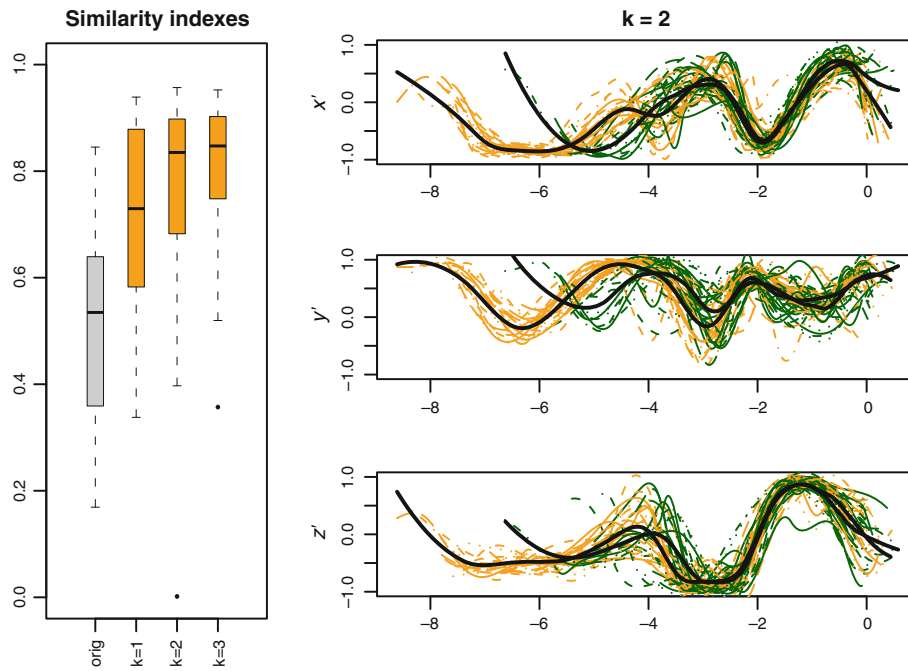


FIG. 4. Left: boxplots of similarity indexes between each curve and the corresponding template for original estimated centerlines and for centerlines aligned and clustered in k groups, $k = 1, 2, 3$. Right: After the alignment, a better clustering is obtained with two groups ($k = 2$), whose templates are represented by the solid thick lines.

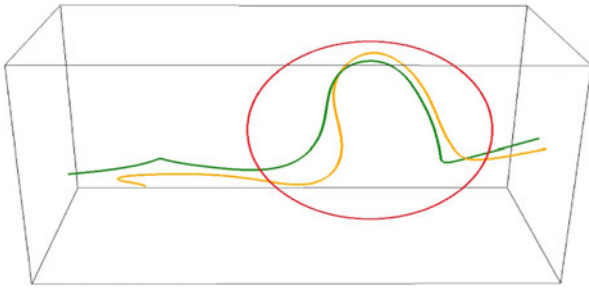


FIG. 5. 3D image of the estimated templates of the two clusters. The dark (green) template is a prototype of Ω -shaped ICA (single-bend siphon), the light (orange) one is a prototype of S-shaped ICA (double-bend siphons).

of principal components) for representing the stochastic functions at hand is data driven: FPCA actually identifies important and uncorrelated modes of variability observed in the data set i.e., eigenfunctions of the sample autocovariance operator. The coordinates of the projections of the data onto the modes in the basis are called *scores*. The statistical relevance of the modes in the basis can be quantified by means of the sample variance of the scores of the projected data i.e. eigenvalues of the sample autocovariance operator. Once dimensional reduction has been achieved, classical multivariate analysis of the scores of the principal components is used to investigate and verify the statistical hypothesis of interest. For an extensive introduction to these techniques we refer to Ramsay and Silverman.²⁹ In particular, we looked for patterns that

discriminate patients in different classes. Discrimination was carried out by an approach called *quadratic discriminant analysis* (QDA), which is a classification rule assuming, for each investigated class, a multivariate Gaussian distribution of the observed features. The basic idea is to calculate the relative proportions of the classes, their means and their covariance matrices with respect to the variables analyzed. For each possible set of features presented by a new subject, Bayes Theorem provides an estimate of his probability of belonging to each one of the groups.

Results of the combined FPCA + QDA analysis on the enriched (geometry + CFD) data set with respect to the classification presented in Table 1 are presented in the next section.

The statistical analyses have been carried out within the statistical programming environment *R*.²⁷

RESULTS

In Fig. 6, ICA radius and curvature, and the local average WSS are presented as functions of the curvilinear abscissa on the centerline. The figure shows the large variability of the data set, even after centerline alignment. It is worth noting that the length of the reconstructed centerlines has also a great variability in the data set. This figure displays, at the top of each plot, a Gaussian kernel estimate of the probability density function of the location of aneurysms along the

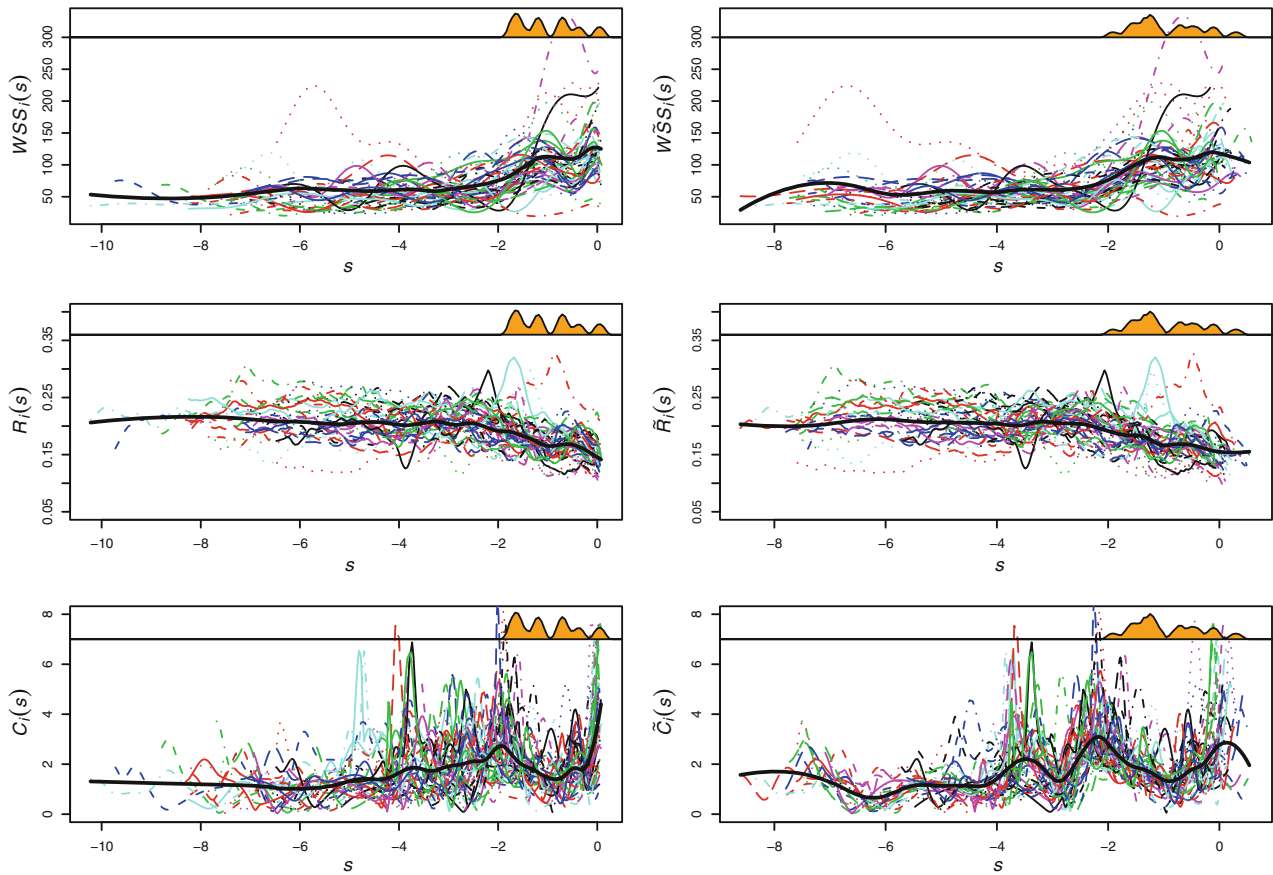


FIG. 6. ICAs \overline{WSS} (top), radius (center) and curvature (bottom) profiles for all subjects respectively before (left) and after (right) registration. Solid black lines show mean curves, as estimated by Loess. On top of each picture is also displayed the estimate of the probability density function of the location of aneurysms along the ICA or at its terminal bifurcation.

ICA or at its terminal bifurcation. Occurrence of the aneurysms in the distal part of the ICA (where tapering is more evident), is almost null at $s \approx -1$ cm. This indirectly identifies the average position of the dural ring the ICA goes through before its terminal bifurcation. Notice that the dural ring is not detectable from images and that aneurysms distal to this position are in general more life threatening.

We concentrated our analysis on the distal ICA, comprising the last 5 cm before its terminal bifurcation, since this was the available tract in all considered patient's 3D models after centerline registration.

A representative subject for each class of Table 1 is presented in Figs. 7–11. On the left column we show the 3D model of the ICA, as defined after reconstruction from images and mesh generation. The magnitude of the computed WSS vector at the systolic peak is plotted on the vascular surface. On the right column we show the morphological and hemodynamical indices evaluated for each subject, expressed as functions of the curvilinear abscissa along the vessel centerline. This sequence of figures highlights the most relevant differences of ICAs in the different groups, by direct comparison.

Notice that only the subject in the LR group presents a significant variation of the \overline{WSS} values along the centerline curvilinear abscissa (Fig. 9) located at the distal half of the main bend. The maximum value of the \overline{WSS} is larger in this case than in all the other considered cases.

As shown in Figs. 10 and 11, the two subjects from the “upper” groups (UN, UR) feature relatively low values of the \overline{WSS} , with no significant variations in the space pattern. The radius of the ICA is consistently larger in the two subjects belonging to groups UN and UR than in subjects belonging to the other groups.

It is also interesting to notice that the computed energy loss is significantly larger in subjects belonging to the No, LN and LR groups, while subjects in the UN and UR groups feature lower values, the p -value of the Wilcoxon test being equal to 0.0030. The difference between the two clusters is remarkable.

FPCA of radius, curvature and \overline{WSS} profiles along aligned ICA centerlines allowed the identification of statistical differences among the five groups of subjects with respect to the principal uncorrelated modes of variability of each quantity of interest. In the first row

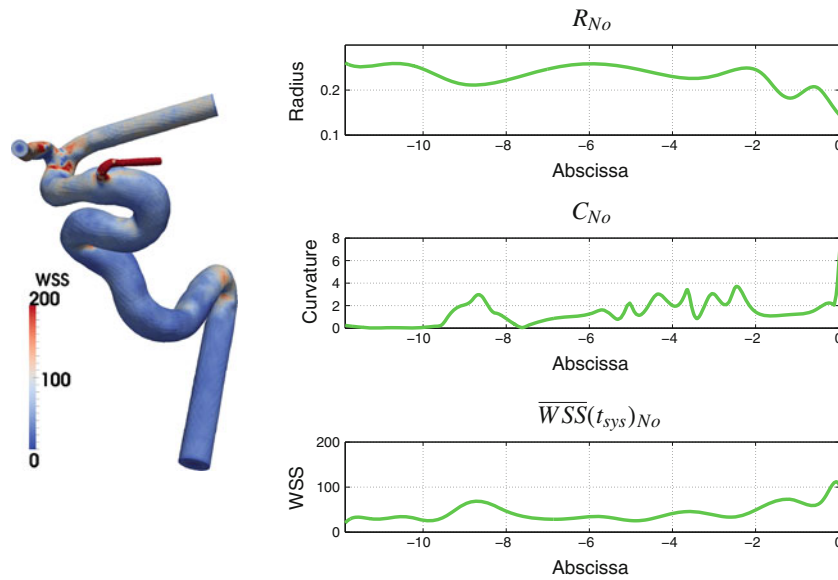


FIG. 7. Representative of group No: the \overline{WSS} at the systolic peak (left); the radius (cm), curvature (cm^{-1}) and \overline{WSS} (dyn/cm²) at the systolic peak as functions of the curvilinear abscissa (right).

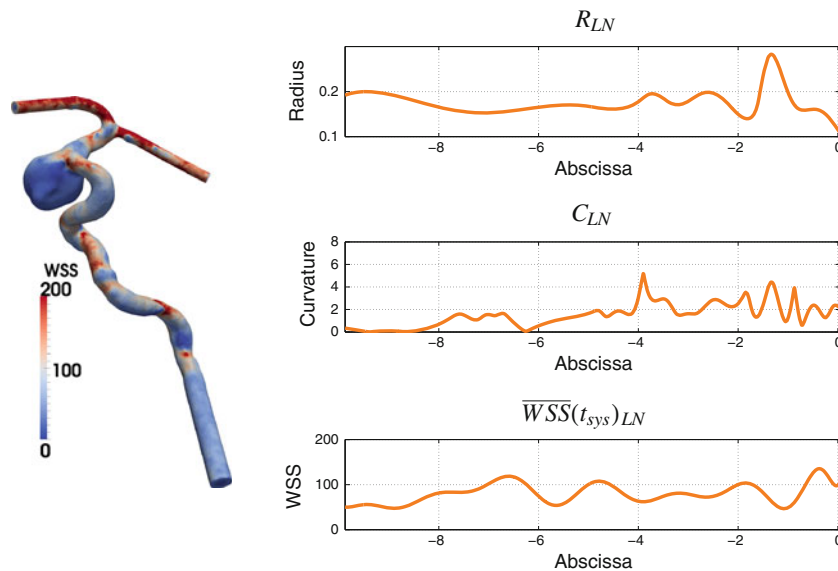


FIG. 8. Representative of group LN: the \overline{WSS} at the systolic peak (left); the radius (cm), curvature (cm^{-1}) and \overline{WSS} (dyn/cm²) at the systolic peak as functions of the curvilinear abscissa (right).

of Fig. 12 we report the profiles of these quantities as a function of the curvilinear abscissa. The second row of the figure displays the projections on the most significant principal components for radius, curvature and \overline{WSS} . Significant differences occur among the five groups of subjects, in particular emphasized by the first principal component of the radius and the curvature and the second principal component of the axial derivative of \overline{WSS} . The third row shows the boxplots of the scores of these principal components for the five groups of subjects. *p*-value in the boxplots is based on the one-sided Wilcoxon test.

DISCUSSION

From the joint morphologic-fluid dynamics analysis, we notice the following facts.

The *first column* of Fig. 12 shows the projections on the first principal component of the ICA radius profiles along aligned centerlines. For each subject, the component along this mode measures the average radius of the ICA; thus, changing the scores with respect to this mode we move from subjects with a narrow ICA to subjects with a wide ICA. As previously pointed out, in Sangalli *et al.*³¹ we already highlighted the significance

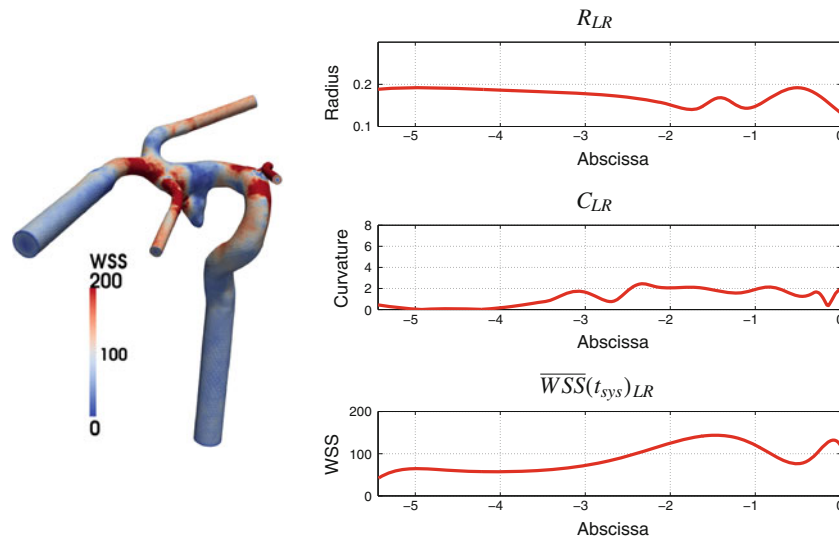


FIG. 9. Representative of group LR: the \overline{WSS} at the systolic peak (left); the radius (cm), curvature (cm^{-1}) and $\overline{WSS}(t_{\text{sys}})_{LR}$ at the systolic peak as functions of the curvilinear abscissa (right).

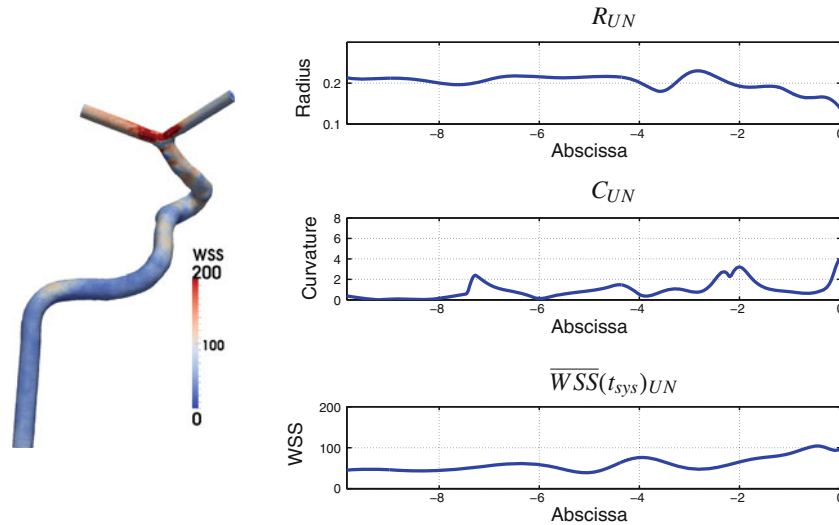


FIG. 10. Representative of group UN: the \overline{WSS} at the systolic peak (left); the radius (cm), curvature (cm^{-1}) and $\overline{WSS}(t_{\text{sys}})_{UN}$ at the systolic peak as functions of the curvilinear abscissa (right).

of the width of the ICA in discriminating among Upper and Lower group subjects. With the present analysis we can more specifically notice that *UN group subjects in particular behave differently from the other four subject groups with respect to this mode of variability, manifesting statistically wider ICAs than the other four groups* (p -value: 0.016).

The *second column* of Fig. 12 shows the projections on the first principal component of the curvature profiles along aligned centerlines. For each subject, the component along this mode measures the prominence of the second peak of curvature of the ICA centerline; thus, changing the scores with respect to this mode we move from subjects with a non particularly evident

second bend of the siphon to subjects with a very marked one. The significance of the presence/absence of the second bend of the siphon is in accordance to what emerged in Sangalli *et al.*³¹ The current analysis refines this result, showing that, the *No* and the *LN* groups behave differently from the other three groups with respect to this mode of variability, being statistically associated to the presence of a double-bend siphon (p -value: ≤ 0.001).

Finally, the *third column* of Fig. 12 shows the projections on the second principal component of the first (axial) derivative of the WSS profiles along aligned centerlines. For each subject, the component along this mode measures the intensity of the WSS peak at the

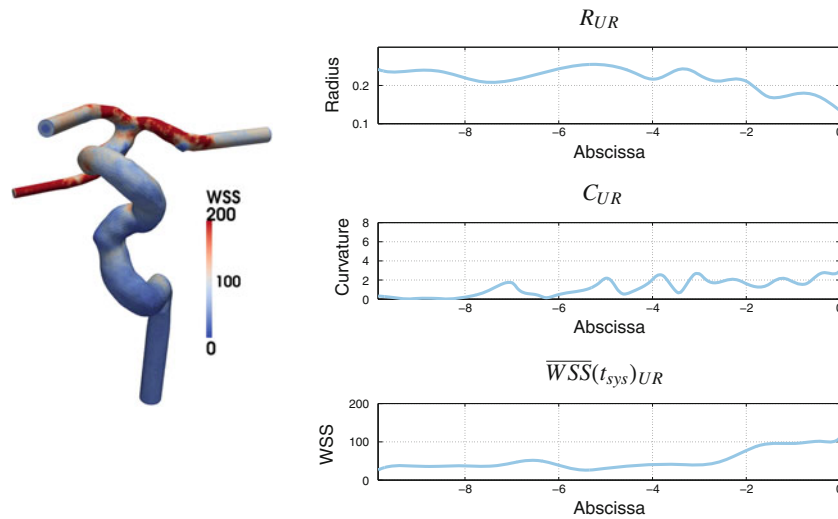


FIG. 11. Representative of group UR: the \overline{WSS} at the systolic peak (left); the radius (cm), curvature (cm^{-1}) and \overline{WSS} (dyn/cm^2) at the systolic peak as functions of the curvilinear abscissa (right).

end of his ICA; thus, changing the scores with respect to this mode we move from subjects with a less pronounced WSS peak to subjects with marked WSS peak. In particular, the **LR** group behaves differently from the other four, manifesting statistically more prominent WSS peaks (p -value: 0.001).

The clustering Ω -S, that—as we have pointed out—has been found here on the basis of a purely statistical argument and then matched with the previous literature, seems also relevant for the aneurysm pathology. As a matter of fact, our previous results showed a statistical evidence of a dependence between cluster membership and aneurysm presence and location.³³ In particular the contingency table (Table 2) shows that all the subjects without aneurysms were found to display S-shaped ICAs; at the opposite, among Upper group subjects only a minority had an S-shaped ICA, whilst the majority (70%) had an Ω -shaped one.

These results pinpoint on the ground of a statistical basis the presence of landmarks with a possible prognostic purpose. A slightly tapered ICA is associated with downstream aneurysms that however do not rupture. High WSS peaks are associated with the rupture of aneurysms hosted by the ICA. The analysis of the curvature suggests that the presence of more pronounced bends in the carotid siphon tends to prevent the onset (S -group) and the rupture (**LN** class) of the aneurysms. Based on these evidences, we formulate the conjecture that the ICA siphon has a protective effect on the intra-cranial arterial tree. In fact, most sites of aneurysm development are inside the dura mater, where arteries float in the subarachnoid space with little or less support from the surrounding tissues, as compared to extradural locations. This could make

them more sensitive to the intensity of flow-induced loads, which are dependent on viscous dissipations in the feeding arteries. Viscous dissipations are induced by flow secondary motions that have a complex dependence on the vessel geometry.¹ In particular, the curvature of the bends of the ICA siphon seems to play a role on viscous dissipations. Whilst S -shaped ICAs are expected to be very effective in dissipating the flow energy, Ω -shaped ICAs would not be as efficient. Other features such as the vessel radius will also be relevant, since ICAs featuring larger values of the radius tend to produce less viscous dissipation.

The conjecture on the dissipative role of the siphon is supported by the computed energy loss featured by the blood stream when flowing through the ICA siphon. This value varies across different groups of subjects. Subjects in the **No** group behave similarly to subjects in the **LN** and **LR** groups, whose flow exhibits greater energy loss (or viscous dissipations) in the ICA siphon. The energy loss (Table 3) discriminates subjects having an aneurysm in the intra-cranial circulation versus subjects with an aneurysm on the ICA or no aneurysm at all (p -value of the one-sided Wilcoxon test 0.003). This is consistent with previous observations in Sangalli *et al.*³³ regarding the role of the ICA curvature. However, this result also suggests that energy losses in the ICA cannot be correctly estimated based on the vessel curvature alone.

Limitations

There are several limitations in this study. The data set is including 52 patients and the statistical significance of the results would be greatly improved by the extension of the number of patients. We are extending

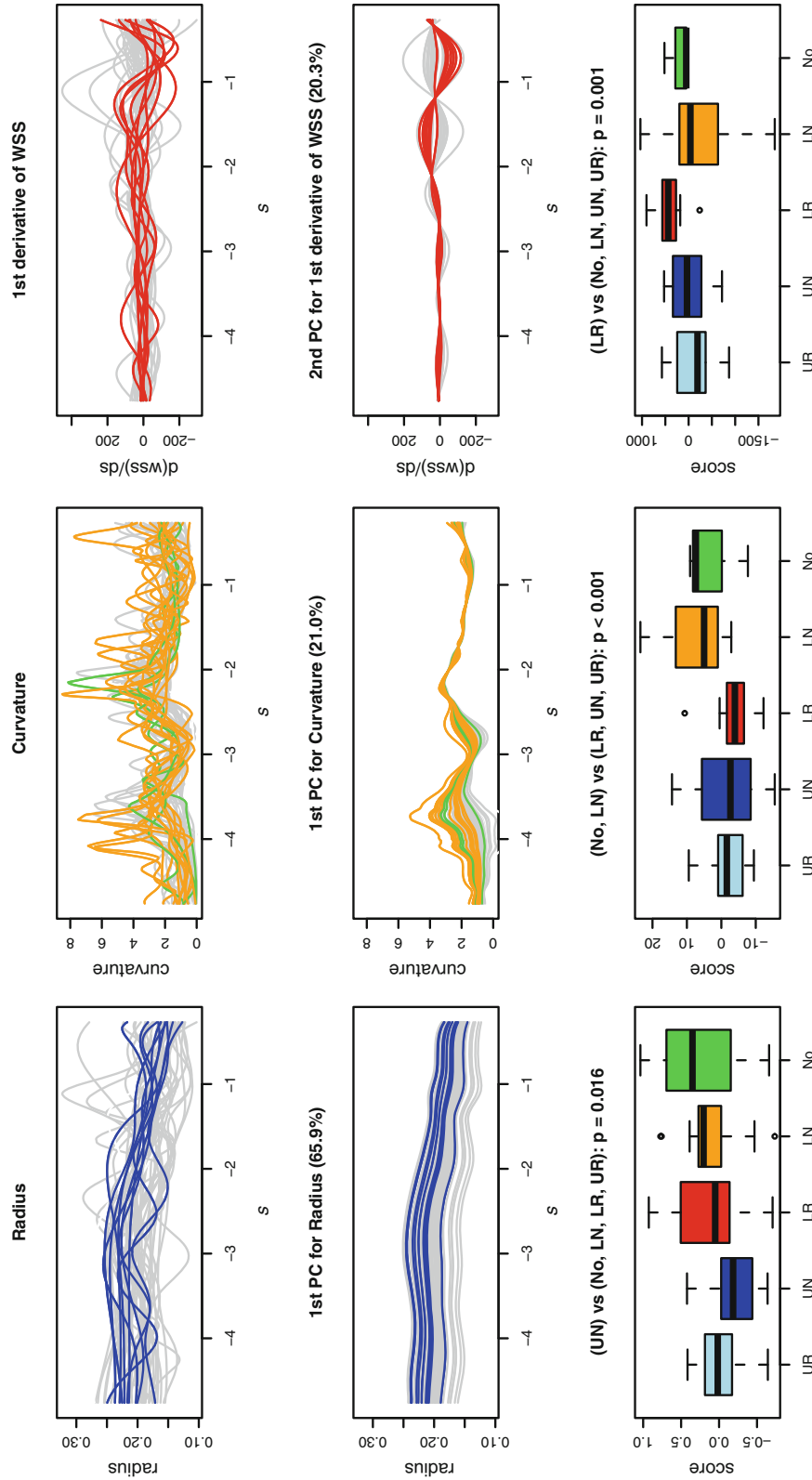


FIG. 12. First column: analysis of ICA radius profiles along aligned centerlines. Second column: analysis of curvature profiles of aligned ICA centerlines. Third column: analysis of the first derivative of the WSS profiles along aligned ICA centerlines. First row: aligned profiles. Second row: projections of subject profiles on the corresponding mode of variability. Third row: boxplots of subject scores on these principal components separated per subject group.

TABLE 2. Conditional contingency table of subjects allocations to Ω -shaped ICAs and S-shaped ICAs clusters.

Position	At/after ICA bifurcation (%)	Along ICA (%)	No aneurysm (%)
Ω	70	48	0
S	30	52	100

TABLE 3. Energy loss computed in the representative subjects for each group. In the last row we report the average \pm the standard deviation for the two macro-groups No,LR,LN and UR,UN, together with the p value of the Wilcoxon test for their statistical difference.

	No	LN	LR	UN	UR	p -value (Wilcoxon)
$\bar{\mathcal{L}}$ (mmHg)	4.47	5.4	4.5	2.74	3.26	
	4.975 \pm 2.113			3.052 \pm 0.565		0.0030

the data set of patients, by including images that will undergo the same procedure described in the paper. In view of a possible cross validation of our results and hopefully to corroborate our conclusions, a web repository of the geometries considered in the present study is under construction.²³ We aim at sharing our data and possibly at receiving more data for incrementing the number of cases of the present analysis.

We have focused the attention on the local average WSS and its axial gradient. These are actually advocated in the literature as principal indicator of different vascular pathologies. However, other indicators could be considered in a similar way, like the Oscillatory Shear Index or the Helicity Factor. On the other hand, it could be interesting to analyze the variation of the local maximum WSS (rather than the local average WSS) as a function of the vessel curvilinear abscissa, to highlight locations that exhibit critical levels of the shear load.

One major improvement of the present study is moreover represented by an integrated analysis of the parent vessel and the sac. The joint analysis of the two regions is anticipated to provide a remarkable insight into the link between the morphology-hemodynamics and the pathology, in particular for a prognostic purpose.

CONCLUSIONS

Despite the limitations of this study, the results presented here clearly point out that the morphology of the ICA and the consequent blood dynamics is likely to play a significant role in the development (and possibly the rupture) of the aneurysm; the possible role

of the siphon in protecting the downstream arterial tree deserves to be further investigated.

An attempt has been made at selecting a reduced set of indicators, able to capture the relevant features for the classification of the data set. Each indicator alone is providing only a partial characterization of the system at hand. The radius profile does not provide information regarding the shape of the cross section, which can be significantly non-circular as pointed out in Piccinelli *et al.*²⁵ The curvature profile does not provide information about the relative orientation of alternating bends in the siphon. The fluid dynamics indicator is based on arbitrary assumptions on the flow conditions at the boundary of the computational domain. However, the assumptions on the simulated flow conditions are made in order to probe different vascular geometries under the same flow regime. Fluid dynamics is here used as a *proxy* for morphology features which are not easy to be measured or interpreted, but affect measurable or computable flow features. Therefore, the rationale behind the joint evaluation of the three indicators is that under the proposed experimental conditions, information provided by fluid dynamics can complement the morphology characterization of subject-specific vascular structures. This eventually leads to the identification of prognostic landmarks. In particular, the results presented here suggest that a single-bend siphon, which is in general detectable from the images, is associated with a higher risk of development and rupture of the aneurysm.

ACKNOWLEDGMENTS

Laura Sangalli is partially supported by the Italian MIUR FIRB research project “Advanced statistical and numerical methods for the analysis of high dimensional functional data in life sciences and engineering”. Marina Piccinelli, Tiziano Passerini and Alessandro Veneziani acknowledge the support of the *Brain Aneurysm Foundation*. All the participants acknowledge the support of the Italian Fondazione Politecnico di Milano and the SIEMENS Medical Solutions, Italy for the support to the *Aneurisk* project (Partners of Aneurisk: MOX—Department of Mathematics, Politecnico di Milano (PI institution), M. Negri Institute, Bergamo, Department of Neurosurgery, Niguarda Ca’Granda Hospital, Milan, Department of Neurosciences, University of Milan, LABS—Department of Civil Engineering, Politecnico di Milano). Alessandro Veneziani wishes to thank Dr. Frank Tong (Emory Hospital) for fruitful discussions. Susanna Bacigaluppi dedicates her contribution to this work to the memory of Dr. M. Collice.

DISCLOSURE OF POTENTIAL CONFLICTS OF INTEREST

All the authors of the present paper declare that they do not have any conflict of interest with the results of the research presented here.

REFERENCES

- ¹Abou-Arab, T. W., T. K. Aldoss, and A. Mansour. Pressure drop in alternating curved tubes. *Appl. Sci. Res.* 48(1):1–9, 1991.
- ²Antiga, L., M. Piccinelli, L. Botti, B. Ene-Iordache, A. Remuzzi, and D. Steinman. An image-based modeling framework for patient-specific computational hemodynamics. *Med. Biol. Eng. Comput.* 46(11):1097–1112, 2008.
- ³Antiga, L., and D. A. Steinman. Robust and objective decomposition and mapping of bifurcating vessels. *IEEE Trans. Med. Imaging* 23:704–713, 2004.
- ⁴Barlow, J. Optimal stress location in finite element method. *Int. J. Numer. Methods Eng.* 10:243–251, 1976.
- ⁵Burman, E., M. Fernandez, and P. Hansbo. Continuous interior penalty finite element method for Oseen's equations. *SIAM J. Numer. Anal.* 44:1248–1274, 2006.
- ⁶Castro, M. A., C. M. Putman, and J. R. Cebal. Patient-specific computational fluid dynamics modeling of anterior communicating artery aneurysms: a study of the sensitivity of intra-aneurysmal flow patterns to flow conditions in the carotid arteries. *AJNR Am. J. Neuroradiol.* 27:2061–2068, 2006.
- ⁷Cebal, J. R., M. A. Castro, J. E. Burgess, R. S. Pergolizzi, M. J. Sheridan, and C. M. Putman. Characterization of cerebral aneurysms for assessing risk of rupture by using patient-specific computational hemodynamics models. *AJNR Am. J. Neuroradiol.* 26:2550–2559, 2005.
- ⁸Cebal, J., F. Mut, J. Weir, and C. Putman. Association of hemodynamic characteristics and cerebral aneurysm rupture. *Am. J. Neuroradiol.* 32(2):264–270, 2010.
- ⁹Chien, A., S. Tateshima, J. Sayre, M. Castro, J. Cebal, and F. Viuela. Patient-specific hemodynamic analysis of small internal carotid artery-ophthalmic artery aneurysms. *Surg. Neurol.* 72(5):444–450, 2009.
- ¹⁰Dhar, S., M. Tremmel, J. Mocco, M. Kim, J. Yamamoto, A. Siddiqui, L. Hopkins, and H. Meng. Morphology parameters for intracranial aneurysm rupture risk assessment. *Neurosurgery* 63(2):185–196, 2008.
- ¹¹Formaggia, L., A. Quarteroni, and A. Veneziani (eds.). *Cardiovascular Mathematics*. Berlin: Springer, 2009.
- ¹²Hoi, Y., H. Meng, S. Woodward, B. Bendok, R. Hanel, L. Guterman, and L. Hopkins. Effects of arterial geometry on aneurysm growth: three-dimensional computational fluid dynamics study. *J. Neurosurg.* 101(4):676–681, 2004.
- ¹³Imai, Y., K. Sato, T. Ishikawa, and T. Yamaguchi. Inflow into saccular cerebral aneurysms at arterial bends. *Ann. Biomed. Eng.* 36(9):1489–1495, 2008.
- ¹⁴Jou, L., D. Lee, H. Morsi, and M. Mawad. Wall shear stress on ruptured and unruptured intracranial aneurysms at the internal carotid artery. *Am. J. Neuroradiol.* 29(9):1761–1767, 2008.
- ¹⁵Krayenbuehl, H., P. Huber, and M. G. Yasargil. *Krayenbuehl/Yasargil Cerebral Angiography*, 2nd edn. New York: Thieme Medical Publishers, 1982.
- ¹⁶LIFEV software. Accessed Dec 23, 2011, from <http://www.lifev.org>.
- ¹⁷Moyle, K., L. Antiga, and D. A. Steinman. Inlet conditions for image-based CFD models of the carotid bifurcation: is it reasonable to assume fully developed flow? *J. Biomech. Eng.* 128:371–379, 2006.
- ¹⁸Nichols, W. W., and M. F. O'Rourke. *McDonald's Blood Flow in Arteries: Theoretical, Experimental and Clinical Principles*. A Hodder Arnold Publication. London: Oxford University Press, 1998.
- ¹⁹Nixon, A., M. Gunel, and B. Sumpio. The critical role of hemodynamics in the development of cerebral vascular disease. *J. Neurosurg.* 112(6):1240–1253, 2010.
- ²⁰Osenberg, H. Simulation des arteriellen blutflusses: Ein allgemeines modell mit anwendung auf das menschliche hirngefasssystem. Ph.D. thesis, Zurich, 1991.
- ²¹Paraview Web Site. Accessed Dec 23, 2011, from <http://www.paraview.org>.
- ²²Passerini, T. Computational hemodynamics of the cerebral circulation: multiscale modeling from the circle of willis to cerebral aneurysms. Thesis, Politecnico di Milano, 2009.
- ²³Passerini, T., M. Piccinelli, and A. Veneziani. Aneurisk repository. Accessed Dec 23, 2011, from <http://ecm2.mathcs.emory.edu/aneurisk/>.
- ²⁴Piccinelli, M., S. Bacigaluppi, E. Boccardi, B. Ene-Iordache, A. Remuzzi, A. Veneziani, and L. Antiga. Geometry of the ICA and recurrent patterns in location, orientation and rupture status of lateral aneurysms: an image-based computational study. *Neurosurgery* 68(5):1270–1285, 2011.
- ²⁵Piccinelli, M., A. Veneziani, D. A. Steinman, A. Remuzzi, and L. Antiga. A framework for geometric analysis of vascular structures: applications to cerebral aneurysms. *IEEE Trans. Med. Imaging* 28(8):1141–1155, 2009.
- ²⁶Prosi, M., K. Perktold, and H. Schima. Effect of continuous arterial blood flow in patients with rotary cardiac assist device on the washout of a stenosis wake in the carotid bifurcation: a computer simulation study. *J. Biomech.* 40(10):2236–2243, 2007.
- ²⁷R Development Core Team. *R: A Language and Environment for Statistical Computing*. Vienna: R Foundation for Statistical Computing, 2010.
- ²⁸Raghavan, M., B. Ma, and R. E. Harbaugh. Quantified aneurysm shape and rupture risk. *J. Neurosurg.* 102(2):355–362, 2005.
- ²⁹Ramsay, J. O., and B. W. Silverman. *Functional Data Analysis*. New York: Springer, 2005.
- ³⁰Rappitsch, G., and K. Perktold. Computer simulation of convective diffusion processes in large arteries. *J. Biomech.* 29(2):207–215, 1996.
- ³¹Sangalli, L. M., P. Secchi, S. Vantini, and A. Veneziani. A case study in exploratory functional data analysis: geometrical features of the internal carotid artery. *J. Am. Stat. Assoc.* 104(485):37–48, 2009.
- ³²Sangalli, L. M., P. Secchi, S. Vantini, and A. Veneziani. Efficient estimation of three-dimensional curves and their derivatives by free knot regression splines, applied to the analysis of inner carotid artery centrelines. *J. R. Stat. Soc. C* 58(3):285–306, 2009.
- ³³Sangalli, L. M., P. Secchi, S. Vantini, and V. Vitelli. Joint clustering and alignment of functional data: an application to vascular geometries. In: *Joint Statistical Meetings Proceedings*, pp. 4034–4047, 2010.
- ³⁴Sangalli, L. M., P. Secchi, S. Vantini, and V. Vitelli. K-means alignment for curve clustering. *Comput. Stat. Data Anal.* 54:1219–1233, 2010.

- ³⁵Sato, K., Y. Imai, T. Ishikawa, N. Matsuki, and T. Yamaguchi. The importance of parent artery geometry in intra-aneurysmal hemodynamics. *Med. Eng. Phys.* 30(6):774–782, 2008.
- ³⁶Schoberl, J. Netgen Web Site. Accessed Dec 23, 2011, from <http://www.hpfem.jku.at/netgen/>.
- ³⁷Sforza, D., C. Putman, and J. R. Cebral. Hemodynamics of cerebral aneurysms. *Annu. Rev. Fluid Mech.* 41:91–107, 2009.
- ³⁸Takao, H., Y. Murayama, Y. Qian, A. Mohamed, W. Matsuda, M. Umezumi, and T. Abe. O-018 a new hemodynamic parameter: energy loss to anticipate aneurysm rupture. *J. NeuroInterv. Surg.* 2(Suppl 1):A8, 2010.
- ³⁹Van Gijn, J., R. S. Kerr, and G. J. Rinkel. Subarachnoid haemorrhage. *Lancet* 369(9558):306–318, 2007.
- ⁴⁰Veneziani, A., and C. Vergara. An approximate method for solving incompressible Navier–Stokes problems with flow rate conditions. *Comput. Methods Appl. Mech. Eng.* 196(9–12):1685–1700, 2007.
- ⁴¹VMTK software. Accessed Dec 23, 2011, from <http://www.vmtk.org>.
- ⁴²Xiang, J., S. Natarajan, M. Tremmel, D. Ma, J. Mocco, L. Hopkins, A. Siddiqui, E. Levy, H. Meng. Hemodynamic-morphologic discriminants for intracranial aneurysm rupture. *Stroke* 42(1):144–152, 2011.
- ⁴³Zienkiewicz, O., R. Taylor, and J. Too. Reduced integration technique in general analysis of plates and shells. *Int. J. Numer. Methods Eng.* 3(2):275–290, 1971.